AIAA 99-0373

Aerodynamic Performance of an NLF Airfoils with Simulated Ice

D.G. Jackson and M.B. Bragg
University of Illinois
Urbana, IL

37th AIAA Aerospace Sciences Meetings & Exhibit

11–14 January 1999/Reno,NV

AIAA-99-0373

AERODYNAMIC PERFORMANCE OF AN NLF AIRFOIL WITH SIMULATED ICE

Darren G. Jackson* and Michael B. Bragg†
University of Illinois at Urbana-Champaign

ABSTRACT

This investigation studied the aerodynamic performance of an NLF(1)-0414F natural laminar flow airfoil with flap deflection and ice accretions. Four models, each incorporating a different ice protection system, were tested in the NASA Lewis Icing Research Tunnel to acquire inter-cycle ice shapes for each ice protection system and a failure mode ice shape. Two-dimensional simulations of the failure-mode and inter-cycle ice accretions were created using stereo lithography and tested in the University of Illinois wind tunnel to acquire C_λ, C_d, C_m and C_h data. Three spanwise cross-sections of the failure-mode ice shape as well as a LEWICE prediction were tested to evaluate the effect of variations in the ice shape along the span of the model. Significant differences were found in the aerodynamic performance. Boundary-layer measurements were made through the use of a boundary-layer mouse and the boundary-layer thickness correlated well to the drag values. Lower surface ice roughness aft of the main accretion was modeled and found to have little measurable aerodynamic effect. All ice accretions tested degraded the aerodynamic performance, but the inter-cycle ice simulations saw larger $C_{\lambda_{max}}$ degradation, compared to the accompanying drag rise, than did the failure-mode ice shapes.

1.0 INTRODUCTION

For over half a century, researchers in aeronautics have studied the characteristics of airfoils. During this time, much knowledge has been gained into the relationship between the airfoil geometry, its pressure distribution, boundary-layer development, and the associated performance characteristics. In recent years, efforts to develop airfoils with low cruise drag coefficients have led researchers toward natural laminar flow (NLF) airfoils.[1] In order to achieve natural laminar flow, these airfoils are designed with a favorable pressure gradient over a large extent of the surface with a short pressure recovery region on the aft portion of the airfoil. This increased efficiency and reduced drag translates directly into reduced fuel usage and improved performance. Laminar flow airfoils present a difficult challenge for the ice protection systems. Laminar flow airfoils require tight surface dimensional tolerances in terms of both waviness and roughness levels in manufacturing in order to achieve the predicted extent of laminar flow. A series of NLF airfoils have been designed by researchers at the National Aeronautics and Space Administration (NASA) Langley Research Center.[1] One concern with these NLF airfoils is their sensitivity to surface roughness. Roughness can come in the form of dirt, insect strikes, ice, or manufacturing irregularities.

The effect of small-scale surface roughness on airfoil performance is well known. The primary effect is to cause premature transition destroying the laminar flow so crucial to the low-drag performance of these NLF airfoils. Some additional pressure drag can be attributed to the roughness as well. Of the roughness previously mentioned, ice accumulation is typically the worst contaminant due to its potentially large size and extent on the airfoil surface. Thus, the purpose of this study was to examine the effect of ice on NLF airfoil performance.

1.1 AERODYNAMIC CHARACTERISTICS OF AIRFOILS WITH RIME AND GLAZE ICE

The aerodynamic penalties due to rime and glaze ice accretions can be quite severe. Typically, glaze ice formations have a more severe effect on the aerodynamic performance than do rime ice formations. This is due in part because rime ice tends to conform to the underlying surface geometry whereas glaze ice often grows horns at oblique angles to the surface. In addition, rime ice usually forms at colder temperatures where the impinging

* Graduate Research Assistant, Department of Aeronautical and Astronautical Engineering, member AIAA.
† Professor, Department of Aeronautical and Astronautical Engineering, Associate Fellow AIAA.

droplets freeze upon impact leaving only a small-scale surface roughness. Glaze ice forms at warmer temperatures where the droplets may not freeze upon impact and often run back along the surface until enough energy is removed for the droplets to freeze. This accretion mechanism results in the large-scale roughness associated with glaze ice.

The effects due to rime and glaze ice on NLF airfoil performance are given in the report by Bidwell.[2] In Bidwell's investigation, both an NLF(1)-0414 airfoil as well as a medium speed airfoil, MS(1)-317, were tested in the NASA Lewis Research Center Icing Research Tunnel (IRT). This is one of the very few NLF airfoil tests performed in the IRT. The results of these tests found that for glaze ice conditions the largest drag increases measured were 486% and 510% for the NLF(1)-0414 and MS(1)-317 respectively. Similarly, for the rime ice condition, the NLF(1)-0414 had a drag increase of 74% while the MS(1)-317 had a drag increase of 122%.

In addition to the drag results, the Bidwell report has some other noteworthy conclusions. The investigation results showed a nonlinear effect of airfoil performance with icing temperature and found that even small variations in the total temperature (±1 °F) can have a significant impact on the ice accretion and its associated drag penalties. When comparing the results due to variations in the ice accretion time, a nearly linear increase in drag was seen with increasing accretion time. Similarly, an almost linear relationship exists between droplet size and drag with the largest droplet sizes producing the largest drag increases. These results agree well with the conclusions drawn from the reports of Shaw and Sotos,[3] Olsen, Shaw and Newton,[4] as well as that of Gray.[5]

Another parameter studied in the Bidwell report was that of angle of attack. For his investigation, both cruise and climb angles of attack were tested. For the glaze ice condition, the highest drag was associated with the ice formation at the cruise condition. This was due to more impingement and ice formation on the upper surface at the cruise angle of attack as compared to the climb angle of attack. For the rime condition, the most significant result was a confirmation of the fact that the minimum drag is found at the ice accretion angle of attack.

1.2 Residual Ice Due to Low-Power De-icing Systems

In order to understand the effects residual icing will have on the aerodynamic characteristics of an airfoil, it is important to understand the typical types and levels of ice formation which remain after the de-icer is cycled. The most recent data source for residual ice quantification is Bond, Shin et al.'s 1990 and 1991 tests in the IRT.[6-9] In these tests a 21-inch chord, 6 foot span, NACA 0012 model with a removable leading edge was tested in glaze and rime icing conditions to document the effectiveness of the various de-icing systems.

Bond's examination of the NACA 0012 at $\alpha = 4°$ illustrated that ice was not completely removed from the pressure side of the airfoil. As noted by Bond and Shin,[7] the low-power de-icing systems are in effect inertia systems. This implies that ice will not be removed if the mass of ice and local velocity is low. At locations where ice was not removed, such as on the lower surface between $x/c \approx 0.05$-0.10, the local velocity around the airfoil is low ($C_p > 0.$). In addition, the local collection efficiencies in this area suggest that the ice mass are also very low.

In the NACA 0012 de-icer tests performed by Bond and Shin, ice thicknesses at the leading edge before de-icing were greater than or equal to 1.2 mm. For the lower surface of the airfoil a typical ice thickness before de-icing was greater than or equal to 0.5 mm. For glaze ice after de-icer implementation the leading edge was effectively cleared of ice by almost all systems; however, several systems had a residual ice thickness greater than or equal to 0.3 mm at the leading edge for the rime ice case. For the lower surface the de-icing was not as effective and a residual ice thickness of greater than or equal to 0.5 mm was observed for practically every de-icing system.

To the authors' knowledge, the only published report to detail de-icer effectiveness on a laminar flow airfoil was the 1981 report by Albright et al.[10] In this report a six-foot section from the root area of a single engine aircraft wing was tested in the IRT with a pneumatic boot installed about the centerline of the wing section. The wing used a NACA 64_2-A215 airfoil at the root which transitioned to the NACA 64_1-A412 airfoil at the tip and incorporated washout of 0.167 deg/foot. The test data contained in the report were sparse due to problems with the IRT tests. In general this tests found problems in de-icing the wing as α, LWC, and MVD were increased.

1.3 Aerodynamic Characteristics of Airfoils with Residual Ice

The initial effect of residual ice roughness is to promote early boundary-layer transition. This will usually cause a drag rise at low lift coefficients and can decrease the maximum lift of some laminar flow airfoils. The drag rise is due to the increased extent of turbulent flow and higher surface shear forces on the airfoil surface while the lift reduction is attributed to early upper surface trailing-edge separation due to a less energetic boundary layer.[11]

The major concern for future aircraft utilizing NLF airfoils is the residual ice effects due to de-icing systems. While the drag of an NLF airfoil with surface roughness will in many cases remain less than the drag on a turbulent airfoil with the same roughness, the percentage increase in drag is higher. Bragg and Gregorek studied

the effects of environmentally imposed roughness on laminar flow airfoils and in general found that with roughness applied laminar and turbulent airfoils are similar in terms of both lift and drag.[11]

The best published data sources found for the aerodynamics of airfoils with residual ice are the 1956 NACA report of Bowden[12] and the 1981 report of Albright, et al.[10] The Bowden report detailed the aerodynamics of a NACA 0011 airfoil model with a pneumatic boot installed while the report of Albright, et. al., focused on a NACA 64_1-412 airfoil (an early NLF design) with a pneumatic boot. The Bowden report provides airfoil performance information as a function of time over two separate 40-minute rime icing encounters while cycling the IPS every 4 minutes. For one rime ice condition (d_{max} = 23μm, LWC=0.5 g/m^3, T_o=10 ºF) at α = 2.3° and 175 mph, the Bowden report finds the sectional drag due to residual ice is increased on average 6.7% above the clean airfoil value while the lift is only slightly less than the clean airfoil value. A more severe rime ice condition (d_{max} = 37μm, LWC=0.5 g/m^3, T_o=10 ºF) at α = 4.6° and V_∞ = 275 mph yielded an average drag increase of 40% and lift decrease of 4.6% due to residual ice. Further testing was done for a glaze ice condition (d_{max} = 37μm, LWC=0.5 g/m^3, T_o=25 ºF) at α = 2.3° and V_∞ = 275 mph over a 32-minute duration while again cycling the IPS every 4 minutes. Here the result of residual ice on the airfoil was to increase the drag by 21.4% and decrease the lift by 1.2%. Another conclusion drawn from the Bowden report concerning residual ice was that the drag seems to increase nearly linearly as the chordwise extent of the residual ice increases.

Data obtained in Albright's tests of the modified 64-series airfoil in the IRT found drag values increased between 40.2% and 93.3% due to icing. After de-icing drag values were between 12.6% and 76.2% higher than the clean airfoil. It is interesting to note that the maximum residual ice drag increase of 76.2% on Albright's NLF airfoil was higher than the maximum value of 41.9% obtained in Bowden's tests.

The data reviewed above detailed airfoil performance with residual ice left on the airfoil immediately after de-icing system activation. A more important case is the so-called inter-cycle ice accretion on the airfoil which is the ice that accretes between cycles of the de-icing system. For example, if a de-icing system is automatically set to activate every one minute, the inter-cycle ice accretion would be the residual ice after an activation, plus the ice that would accrete in the next one minute before the next scheduled activation of the de-icing system. Inter-cycle ice has received attention only in the last couple of years and to the authors' knowledge very little ice accretion or performance data on these accretions is available in the literature.

Some limited inter-cycle data was found in the Bowden report for the rime and glaze ice conditions mentioned earlier. For the rime ice condition at α = 2.3° and 175 mph, the Bowden report finds the sectional drag due to inter-cycle ice is increased an average of 16.7% over the clean airfoil condition while the lift was reduced 2.6%. This is over twice as severe as the performance penalties associated with the residual ice. The more severe rime ice at α = 4.6°and V_∞ = 275 mph had a drag increase of 60% and a lift decrease of 5.8% from inter-cycle ice which is significantly higher than that seen for the residual ice. For the glaze ice condition at α = 2.3° and V_∞ = 275 mph, a drag increase of 71.4% and lift decrease of 5% were seen due to inter-cycle ice accretion. The performance degradation associated with this condition is over three times that for the residual ice. However, performing a similar glaze ice test using a 1-minute cycle time yields a drag increase of 47.1% and a lift decrease of 3.5%. Thus, as would be expected, reducing the cycle time reduces the aerodynamic penalty associated with the inter-cycle ice accretion.

In light of the severe penalties that inter-cycle ice can have on airfoil performance, this report seeks to quantify the characteristics of inter-cycle ice on an NLF airfoil and the resultant airfoil performance. Additionally, this investigation also seeks to determine the accuracy with which the current simulation methods can model the natural ice accretion phenomenon.

2.0 Experimental Method

2.1 Airfoil and Wind Tunnels

The airfoil section used for this investigation was the NLF(1)-0414F. The airfoil was designed for a C_l = 0.40-0.45 at a Reynolds number of 10 x 10^6 and M ≤ 0.40 with a thickness of 0.143 chord. Laminar flow was achieved back to 70 percent chord on both the upper and lower surfaces through the use of accelerated flow over much of the airfoil surface with a pressure recovery aft of the 70 percent chord location. More information on the design of this airfoil can be found in NASA TM 85788.[1]

The wind tunnel testing performed for this investigation was conducted in two separate facilities. First, testing was done in the NASA Lewis IRT. The IRT has a 6 ft. x 9 ft. cross-section and is capable of producing conditions representative of typical icing clouds. This testing was performed on four NLF(1)-0414 models with a chord of 4 ft. and a span of 6 ft. Each model was equipped with a different ice protection system (IPS).

The second part of the testing was performed at the University of Illinois at Urbana-Champaign (UIUC) Subsonic Aerodynamic Laboratory's 3 ft. x 4 ft. Low-Speed Low-Turbulence (LSLT) wind tunnel. The model was an 18-inch chord NLF(1)-0414F spanning 33.6 inches with a 25% chord flap. In an effort to increase repeatability across facilities, the flap gap was sealed on the lower surface using a Mylar strip, placed so that it

would not influence the hinge moments. The model was also equipped with 97 pressure taps located to resolve the gradients in the pressure distribution.

The simulated ice accretions were manufactured using stereo lithography which produced very accurate simulations of the ice shape contour. For this method, the ice accretion tracings from the IRT were digitized to produce coordinates of the ice shape profile. Since the ice shape was to span 33.6 inches, a two-dimensional extrusion of the ice shape profile was created. Due to manufacturing constraints, the simulated ice shapes had to be made in four sections. For the failure mode ice shape, there was concern that the ice shape may not support the applied load, thus two steel rods of 1/8 inch diameter were inserted through the ice shape to help provide additional rigidity as well as align the four sections. To attach these large ice shapes to the model, steel endplates were incorporated into the ice shapes that were screwed into the ends of the model leading edge. For the inter-cycle ice shape cases, attachment was accomplished using 0.002-inch thick double-sided adhesive transfer tape. The transfer tape was used to help hold the large ice shapes as well.

During the UIUC wind tunnel testing of these simulated ice shapes, an effort was made to reproduce the conditions as seen in the actual ice accretions; therefore, the ice roughness seen on the lower surface aft of these ice shapes was modeled using grit roughness (see Table 1). For the large ice shapes #14 grit ($k \cong 0.066$") was used to represent the ice feathers seen aft of the large horn. Similarly, the ice roughness seen behind the main inter-cycle ice shapes was simulated using #20 grit ($k \cong 0.047$") roughness. The chordwise extent and densities for each of these roughness simulations were determined from digital photographs taken during the IRT test (see Table 1).

2.2 IRT DATA ACQUISITION

The first step in this investigation was performed in the NASA Lewis IRT on the full-scale NLF models to determine the icing characteristics of this airfoil with and without ice protection. All four IPS systems were tested under the same conditions. These conditions, typical of a general aviation aircraft in an icing encounter, were as follows:

LWC = 0.7 g/m^3	V = 156 mph
MVD = 20 μm	Time = 10 min.
T_o = 24 °F	α = 1°

The IPS devices were each activated (or cycled) in 1 minute intervals. The last activation of the IPS was 1 minute prior to the end of the ice accretion. This was done so that the largest accretions seen between de-icing cycles (inter-cycle ice) could be measured. A typical inter-cycle ice accretion is shown in Fig. 1. Once each run had finished, tracings were taken at 3 spanwise locations: one at the midspan, one 6 inches above and one 6 inches below midspan. The tracings were made by melting a slot in the ice at the desired location, placing a template in the slot, and tracing the shape of the ice onto the template by hand. To complete the ice accretion tests, tracings for a 45-minute accretion without IPS operation at the same LWC, MVD, T_o, and airspeed were collected (see Fig. 2). This condition was representative of a failure of the IPS while the aircraft maintained a holding pattern.

2.3 UIUC DATA ACQUISITION

The other part of this investigation was performed in the UIUC LSLT wind tunnel. The goal of these tests was to take extensive aerodynamic measurements of simulated ice shapes constructed from the tracings obtained in the IRT. While analyzing the tracings taken during the IRT tests, it was decided that for the residual ice shapes, only the midspan tracings would be used. Although there was nonuniformity in the residual ice over the span, it was felt that the midspan location was representative of the ice levels seen. For the failure-mode ice shape, a notable variation of the ice shape across the span was seen (see Fig. 2). Since the accretion was intended to be two-dimensional, it was decided to quantify the effects due to the variation of the icing cloud. Therefore, all three spanwise locations were chosen for testing. For additional comparison, a LEWICE representation of the failure-mode ice shape was created at NASA Lewis Research Center and selected for testing.

The lift, drag and pitching moment were measured in the UIUC tunnel using a force/moment balance shown in Fig. 3. The balance was contained in a turntable system that allowed positioning of the model to the desired angle of attack. Drag was also measured using a traversing wake rake with 59 total pressure probes and 3 static probes. The wake pressures and surface static pressures were measured using an electronically scanned pressure (ESP) system. Model surface pressures were integrated to provide lift, moment and hinge-moment data. The flap was actuated by a two-arm linkage driven by a linear traverse system that was mounted on the metric force plate of the balance. A load cell was incorporated into one of the arms and measured the flap hinge moments.

To complement the force and moment measurements, boundary-layer velocity profile measurements were taken in the UIUC LSLT wind tunnel on the 18-inch chord model. The boundary-layer mouse consisted of an array of 34 total pressure probes supported by a thin steel plate situated with a hinge allowing the plate to rotate. This provided the necessary flexibility to resolve thin clean-airfoil boundary layers as well as thick boundary layers seen on models with large ice shapes. The boundary-layer mouse is shown attached to the model in Fig. 4. The majority of the probes were set 1/16 inch center-to-center with a few near the model surface having a tighter

spacing. A single static-pressure probe was placed on the outer edge of the array to measure the static pressure in the boundary layer. The use of a single static probe was based on the standard boundary-layer theory assumption that the static pressure is constant through the boundary layer. For these measurements, the mouse was placed on the upper surface at x/c = 0.65.

In this paper data for the model (with and without ice) tested over an angle of attack range from –10° to 18° at a Reynolds of 1.80×10^6 are presented. In all cases, surface pressures and force/moment balance measurements were taken along with the wake survey and boundary-layer mouse. However, in this report, drag values shown are taken from the wake survey and lift, pitching moment, and hinge moment are taken from the force/moment balance. Although this constitutes the majority of the data taken at UIUC, these methods do not provide a very detailed understanding of the flow over the model surface. To provide that information, a fluorescent oil flow visualization technique was utilized.

This flow visualization technique is based on the differences in surface shear stress associated with laminar, turbulent and separated flows. Laminar flows, in general, have lower shear than do turbulent flows. Thus, in turbulent flow regions, the oil is scrubbed away more quickly than in the laminar regions. This results in less oil film remaining to fluoresce, thus appearing darker. In a similar manner, areas of separated flow are distinguished usually by three key features. First, there is usually a region of pooled oil due to zero shear at the separation point. Secondly, for a reattaching bubble there is the reattachment location indicated by a high shear area aft of the reattachment. Lastly, there is occasionally a reverse flow region inside the separation bubble where the flow moves upstream along the surface from the reattachment line until the shear becomes zero and it can no longer move forward. In order to understand the flow over the surface of the model under clean and contaminated conditions, flow visualization was performed for the clean model and with the failure mode ice shapes. This allowed a mapping of the laminar, turbulent, and separated flow regions for each of the cases tested.

2.4 Data Reduction and Uncertainty

The lift coefficient (C_λ) and pitching moment coefficient (C_m) measurements were taken with the force/moment balance and the surface pressure measurements. The primary drag coefficient (C_d) measurements were taken with the wake rake and confirmed with the force/moment balance. The flap hinge moment coefficients (C_h) were measured with the flap hinge load cell and confirmed with surface pressure measurements. The surface pressure measurements and fluorescent oil flow visualization were used to determine the location of the separation bubbles and for flow diagnostics.

The C_λ, C_m, and C_d from the pressure and force balance measurements were calculated using standard methods with conventional definitions, e.g. the C_m was defined about the quarter chord and the C_h was obtained by determining the trailing-edge-down moment about the flap shaft and non-dimensionalizing by the flap surface area and the flap chord length. All of the aerodynamic coefficients were corrected for wall effects using the method of Rae and Pope.[13]

Shown in Table 2 are the uncertainty estimates of the aerodynamic coefficients for a typical data point. The cases shown are for the clean model at $\alpha = 0°$ with zero flap deflection and $Re = 1.80 \times 10^6$. This condition was selected because it was located in the typical operating range for this airfoil.

3.0 Results and Discussion

The results of the aerodynamic tests are presented and discussed here and divided into 4 sections. The model without ice is discussed first followed by the results with the large glaze failure-mode ice simulation, and simulated inter-cycle ice. In the last section the results for the different types of ice are compared.

3.1 Clean and Tripped Airfoil

The aerodynamic performance of the NLF(1)-0414F airfoil as measured in the UIUC wind tunnel is shown in Fig. 5. Here the lift, drag and moment coefficient data are shown for the model with natural transition (clean) and with transition artificially fixed (trip case) at 7% chord on the upper and lower surfaces. All the data shown was acquired at $Re = 1.80 \times 10^6$. The computational results from the XFOIL[14] airfoil analysis code are also shown for comparison.

The NLF(1)-0414F airfoil was designed to achieve laminar flow by having a slightly favorable pressure gradient followed by a rapid pressure recovery from 70% chord to the trailing edge. In this test the airfoil is operated at a Reynolds number well below the design value and has a trailing-edge flap which starts at 75% chord. The flap places a discontinuity in the airfoil surface in the rapid pressure recovery region.

The “kink” or bend in the measured clean lift curve at 3 deg. AOA is associated with the onset of trailing-edge separation from approximately the 70% chord location. XFOIL cannot model the flap discontinuity and fails to properly model the flow separation on the aft part of the airfoil. Note the divergence of the experimental and XFOIL lift values above 3 degrees. This results in XFOIL not only overpredicting the maximum lift coefficient, $C_{\lambda_{max}}$, but also the lift curve slope as well.

The minimum measured drag coefficient was approximately 0.006 at a Reynolds number of 1.80 $x10^6$. XFOIL predicted the clean airfoil drag values fairly well until stall was approached. There existed a shift in the drag values between –4 and +4 degrees angle of attack. This could have been a model misalignment problem, but since it did not appear in the lift, it is probably another indication of the problem predicting the separation on the aft part of the airfoil.

The moment coefficient comparisons are shown in Fig. 5c. As with the drag values, the experiment and XFOIL compared reasonably well on the clean model, but not for the tripped case. The pitching moment is seen to be a minimum at $\alpha = 3°$ for the experimental cases and the clean XFOIL data. This is another indication of the separation in the upper surface recovery region on the airfoil and corresponds to the change in lift curve slope seen in Fig. 5a.

3.2 FAILURE-MODE GLAZE ICE SHAPES

The IRT tracings from the IPS failure-mode ice accretions are shown in Fig. 6. The failure case produced the large glaze accretions shown which are compared to the LEWICE prediction. Tracings were taken at three spanwise stations on the model. They were centered about the model and tunnel centerline located 36 inches above the tunnel floor and spaced 6 inches apart. As the spanwise location moves from the 30-inch to the 42-inch location, the upper-surface glaze ice horn can be seen to reduce in length and move closer to the extended chord line. The upper horn for the LEWICE shape has a location between the 36- and 42-inch experimental values and a horn length slightly larger than the 30-inch shape. The lower-surface horns from the measured shapes are very similar, with the LEWICE case being somewhat underpredicted.

The aerodynamic performance of the NLF(1)-0414F airfoil with these 4 glaze ice shapes, simulated using stereo lithography, is shown in Figs. 7a to 7d. The lift, drag and pitching moment coefficients were all significantly affected by the simulated ice accretions. The lift curve slopes in Fig. 7a were reduced slightly by all of the ice shapes, but the most significant change was in $C_{\lambda max}$. The maximum lift was reduced, as was the angle of attack for maximum lift. The two largest ice shapes have similar lift performance with a $C_{\lambda max}$ of 0.75 (a 42% reduction) and a reduction in stall angle from 13 degrees to 5 degrees. The LEWICE shape has performance similar to the 42-inch ice shape with $C_{\lambda max}$ around 0.90. Thus the degradation in lift performance is largest for the larger ice shapes as expected. The LEWICE shape matches closely the lift of the 42-inch shape that has a similar horn angle but a significantly shorter horn length.

The drag values show large increases in drag with the measured shapes while following the expected pattern of the largest shape (30-inch) having the largest drag. The largest drag rise seen at $\alpha = 0°$ was from 0.0060 on the clean model to 0.060 with the 30-inch ice simulation, a 900% increase. For positive angles of attack, the LEWICE drag coefficient lies between the 36 and 42-inch shapes which bound the LEWICE shape with respect to the upper horn angle. However, note that at negative angles of attack the LEWICE shape has less drag than expected. This is due to the underprediction of the lower horn length.

The pitching moment coefficient curves in Fig. 7c show large variations in the C_m with α due to the simulated ice accretions. From $\alpha = 0°$ to $\alpha = 5°$ the C_m becomes much more positive (nose up) as the separation bubble aft of the ice shape upper horn is growing rapidly. At $\alpha = 5°$, where the airfoil maximum lift occurs, a sharp nose-down break occurs due to the stalling process. Again, the curves roughly follow the trends in ice shape size and horn location discussed earlier.

The hinge-moment data in Fig. 7d shows a much less dramatic effect. This is probably due to the severe adverse pressure gradient over the flap in the clean case that leads to flow separation over the flap at even moderate angles of attack. This may be dominating the pitching moments and not be significantly altered by the ice shapes. A study of the surface pressure distributions and flow visualization data may help explain this effect as analysis of this data set continues.

The boundary-layer profiles for these large ice shapes produced a boundary-layer thickness that was between 1" and 2" as compared to the clean model that had a boundary-layer thickness of around 0.1". A set of boundary-layer velocity profiles at $\alpha = 0°$ and Re = $1.80x10^6$ taken with the boundary-layer mouse are shown in Fig. 8. The boundary-layer thickness followed the trends in the measured drag for the ice shapes with the 30-inch shape having the thickest boundary layer and the 42-inch shape the thinnest.

The feathers and other lower surface roughness features not represented in the ice shapes were simulated by applying grit roughness to the airfoil in the locations given in Table 1. Figure 9 shows the lift performance of the airfoil with the 30-inch ice shape with no roughness and with 2 different roughness densities of the #14 grit. The roughness was seen to have almost no effect on the lift performance of the airfoil with ice. This is not surprising as the roughness was on the lower surface and aft of the large lower surface horn. This region of the flow was separated at all but the highest angles of attack, thus placing the roughness in a nearly dead-air region. The effect on the other aerodynamic parameters was equally as small. Figure 10 presents measured boundary-layer profiles for the 30 and 36-inch simulated ice shapes with and without lower-surface roughness. Again the influence is minimal. These and many other similar experiments showed that the lower surface roughness aft

of the horn had a negligible effect on the aerodynamic performance and did not require careful modeling. This differs from the results obtained by Olsen, Shaw, and Newton. During actual ice accretion tests they removed the lower surface ice feathers and noted the changes in the measured drag. For the 5-minute glaze ice condition they tested, a decrease in drag from 424% (as compared to the clean airfoil) to 361% was seen after removal of the ice feathers. Similar decreases were seen with removal of the feathers aft of 5-minute rime ice accretions. For one rime condition the drag increase over the clean airfoil was reduced from 120% to 14.5%. The reason for the significant difference in results obtained at UIUC is that the 45-minute ice accretion tested at UIUC created a large separation bubble aft of the ice shape effectively reducing the impact of roughness in this location.

A flow visualization photograph of the upper surface of the airfoil with the 30-inch glaze ice shape is shown in Fig. 11. Here the flow is from right to left and the numbers displayed in the lower portion of the photo are the x/c location in percent chord. The vertical white strip on the right side of the photo is the top view of the upper horn from the ice simulation where point A denotes the aft end of the ice shape. The flow separates from the forward tip of the ice horn forming a separation bubble. At this angle of attack the bubble reattaches at 22% chord, seen as the faint vertical line in the oil flow at point C. Reverse flow exists on the surface from point C to B until the reverse flow separates at point B as it experiences an adverse pressure gradient while approaching the ice shape. The line at point D is due to the flap gap.

3.3 Inter-cycle Ice Shapes

The 4 inter-cycle ice shapes tested are shown in Fig. 12. While the actual ice accretions were 3-D (see Fig. 1), the shapes were simulated as 2-D extrusions of the tracings shown with and without roughness added. No clearly defined horns are seen in any of the shapes with only a relatively thin irregular layer of ice over the leading edge.

All ice shapes reduced the maximum lift and stall angle as shown in, Fig 13a. The IPS 3 case caused the largest reduction with a $C_{\lambda_{max}} = 0.90$ or a reduction of about 30%. The angle for maximum lift was reduced by 6°. IPS 1, 2 and 4 had similar but lesser effects on the lift. The IPS 3 shape had a sharp peak of ice which was significantly thicker than the other accretions. Looking at the results provided in the Bowden report, the lift performance data is limited to only one angle of attack and no results regarding $C_{\lambda_{max}}$ can be derived. However, from the data provided in the report it can be seen that lift decreases between 3-5% are typical. The UIUC data shows a larger decrease in lift at this angle of attack. A decrease of 11.7% is seen as the removal of the separation bubble due to the ice shape removes the kink in the lift curve. At higher Reynolds numbers near the design conditions, the separation bubble would not be present. Thus, changes in the lift curve slope would likely not occur and only changes in $C_{\lambda_{max}}$ would be seen.

The drag coefficients in Fig. 13b show that the inter-cycle ice increased the drag significantly as expected. As the lift increased with α the drag of the IPS 3 simulation was significantly higher than the other shapes. The trends at negative α's were different, as the lower surface accretions became more important. Looking at the UIUC results at $\alpha = 2^{o}$, a drag increase between 149% and 246% were seen with the IPS3 ice shape having the most significant change in performance. These increase are three to five times that seen by Bowden.

Unlike the large glaze failure-mode shapes, the smaller inter-cycle shapes had a less dramatic effect on the pitching moment, Fig. 13c. For $\alpha > 2°$ the iced and clean airfoil pitching moments follow similar trends. The iced cases are displaced up reflecting a more nose-up moment until the stall process begins on the inter-cycle ice cases. As the iced cases stall earlier, a large decrease in the pitching moment (nose down) was measured as the airfoil stalls and increased suction was developed on the aft upper surface. As before, the hinge moments were not significantly affected, Fig. 13d.

The boundary-layer velocity profiles at $\alpha = 0°$ show a significantly thicker boundary layer for the IPS 3 case, Fig. 14. The IPS 3 boundary layer is over twice as thick as that for the other 3 simulated inter-cycle ice cases. This is consistent with the larger effect this shape has on the aerodynamic performance.

As with the failure-mode glaze shapes, grit roughness was added to the inter-cycle ice shapes to simulate the smaller roughness not modeled by the shape. Figure 15 shows the lift performance of the airfoil with IPS 1 and 3 shapes with and without grit roughness added. The grit used was #20 in size and the densities used were intended to simulate the density seen on the actual accretions (see Table 1). The reduction in $C_{\lambda_{max}}$ due to addition of roughness was minimal. In nearly every case, a small increase in drag was seen with the addition of roughness on the lower surface aft of the ice shape (data not shown). The stall angle, the AOA at which the break in the moment curve occur, etc. seemed to be unaffected by the addition of roughness as well.

3.4 Simulated Ice Comparison

In Figs 16 a – d the aerodynamic performance for a representative sample of the cases tested are shown. This includes the clean and tripped airfoil, the inter-cycle ice case IPS3, the 30-inch failure mode glaze shape and data obtained for #80 grit sandpaper. The purpose of the sandpaper tests was to provide data for a standard roughness that would represent initial ice accretion roughness and could be easily duplicated. The sandpaper

was placed around the leading edge from x/c = 0.07 on the lower surface to x/c = 0.07 on the upper surface.

All the cases show a reduction in $C_{\lambda_{max}}$ compared to the clean case with the tripped airfoil $C_{\lambda_{max}}$ only slightly lower and the 30-inch ice shape showing a large reduction. The inter-cycle ice simulation has a very large loss in $C_{\lambda_{max}}$ considering it is only a 1-minute accretion and the 30-inch failure case represents a 45-minute accretion. From $-5° \le \alpha \le 0°$ the drag values for all the ice simulations except the 30-inch case are very similar at about 0.0150, Fig 16b. However, the 30-inch failure case has drag values from 0.105 to 0.060 in this angle of attack range. For positive angles of attack the IPS3 case has significantly larger drag than the other cases. While the $C_{\lambda_{max}}$ value for the 30-inch shape is somewhat less than the IPS3 case, the drag coefficient for the large glaze case is much larger.

The pitching moments for all but the 30-inch glaze case are well behaved and follow the expected trends due to an early stall. The 30-inch case shows large changes in C_m due to the large separation bubbles generated by the large upper and lower surface ice horns. At positive angles of attack only small changes in the hinge moment coefficient are found as seen in Fig. 16d.

4.0 CONCLUSIONS

Several important observations can be drawn from this research.

1. The use of stereo lithography proved to be a convenient and accurate method for generating simulated ice accretions.
2. The spanwise differences in the ice shapes resulted in significant differences in the aerodynamic performance.
3. Large C_m but only small C_h effects were found due to the failure-mode ice accretions.
4. The boundary-layer mouse data showed that increased boundary-layer thickness correlated well to drag coefficient.
5. Surface roughness on the lower surface aft of the ice shape simulation had little effect on aerodynamic performance.
6. Simulated inter-cycle ice (2-D simulation) had a 150% drag rise compared to a 900% increase for the failure shape case; however, the $\Delta C_{\lambda_{max}}$ values were approximately 30% and 40%, respectively. Thus, inter-cycle ice had a relatively large effect on maximum lift of the airfoil.

5.0 ACKNOWLEDGMENTS

This work was supported under a NASA grant. The authors would like to acknowledge the support of Dr. David Anderson, Mr. Tom Bond, Mr. Andrew Reehorst, Ms. Tammy Langhals, and Dr. William Wright from NASA Lewis Research Center. The authors would also like to express appreciation to Mr. Kristian Engelsen and Mr. Steven Fennell from UIUC for their assistance during this investigation.

6.0 RFERENCES

[1] McGhee, R. J., Viken, J. K., Pfenninger, W., Beasley, W. D., Harvey, W. D., "Experimental Results for a Flapped Natural-Laminar-Flow Airfoil with High Lift/Drag Ratio", NASA TM 85788, May 1984.

[2] Bidwell, C. S. "Icing Characteristics of a Natural-Laminar-Flow, a Medium-Speed, and a Swept, Medium-Speed Airfoil", 29th Aerospace Sciences Meeting, AIAA-91-0447, Reno, NV, January 7-10, 1991.

[3] Shaw, R. J., Sotos, R. G., "An Experimental Study of Airfoil Icing Characteristics", NASA TM 82790, 1982.

[4] Olsen, W., Shaw, R. J., Newton, J. E., "Ice Shapes and the Resulting Drag Increase for a NACA 0012 Airfoil", NASA TM 83556, 1982.

[5] Gray, V. H., "Predictions of Aerodynamic Penalties Caused by Ice Formations on Various Airfoils", NASA TN D-21660, 1964.

[6] Shin, J. and Bond, T.H., "Surface Roughness Due to Residual Ice in the Use of Low Power Deicing Systems", 31st Aerospace Sciences Meeting & Exhibit, AIAA-93-0031, Reno, NV, January 11-14, 1993.

[7] Bond, T. H. and Shin, J. "Results of Low Power Deicer Tests on a Swept Inlet Component in the NASA Lewis Icing Research Tunnel", 31st Aerospace Sciences Meeting & Exhibit, AIAA-93-0032, Reno, NV, January 11-14, 1993.

[8] Bond, T. H., Shin, J., Mesander, G. A., "Advanced Ice Protection Systems Tests in the NASA Lewis Icing Research Tunnel", NASA TM 103757, Presented at the 47th Annual American Helicopter Society Forum and Technology Display, Phoenix, AZ, May 1991.

[9] Bond, T. H., Shin, J., Mesander, G. A., and Yeoman, K. E., "Results of the USAF/NASA Low-Power Ice Protection Systems Test in the NASA Lewis Icing Research Tunnel", NASA TP-3319, Sept. 1993.

[10] Albright, A. E., Kohlman, D. L., Schweikhard, W.G., and Evanich, P., "Evaluation of a Pneumatic Boot Deicing System on a General Aviation Wing Model", NASA TM-82363, June 1981.

[11] Bragg, M. B. and Gregorek, G. M., "Environmentally Induced Surface Roughness Effects on Laminar Flow Airfoils: Implications for Flight Safety", AIAA paper 89-2049, AIAA/AHS/ASEE Aircraft Design, Systems, and Operations Conference, Seattle, WA, July 31 - Aug. 2, 1989.

[12] Bowden, D. T., "Effect of Pneumatic De-Icers and Ice Formations on Aerodynamic Characteristics of an Airfoil", NACA TN 3564, Feb. 1956.

[13] Rae, W. H. and Pope, A., *Low-Speed Wind Tunnel Testing*, John Wiley & Sons, 1984.

[14] Drela, M., "XFOIL 6.6 User Primer", MIT Aero and Astro Engineering, March 14, 1996.

Table 1. Roughness simulations on lower surface aft of main ice shape.

Ice Simulation	Grit Number	k (Inches)	From (x/c)	To (x/c)	Area Density
30-Inch	14	0.0661	0.0298	0.1604	17%
36-Inch	14	0.0661	0.0288	0.1594	17%
42-Inch	14	0.0661	0.0088	0.1394	17%
LEWICE	14	0.0661	0.0417	0.1723	17%
IPS1	20	0.0469	0.0251	0.1084	9%
IPS2	20	0.0469	0.0263	0.1713	16%
IPS3	20	0.0469	0.0000	0.1272	33%
IPS4	20	0.0469	0.0168	0.1418	38%

Table 2. Experimental uncertainties for the clean model at $\alpha = 0°$ and $\delta_f = 0°$ at Re=1.80x10^6.

Aerodynamic Coefficients	Reference Value	Absolute Uncertainty	Relative Uncertainty
C_l Balance	0.49439	0.00219	0.44%
C_d Pressure	0.00690	0.00010	1.40%
C_m Balance	-0.07668	-0.00033	0.43%
C_h Balance	-0.06622	-0.00175	2.64%

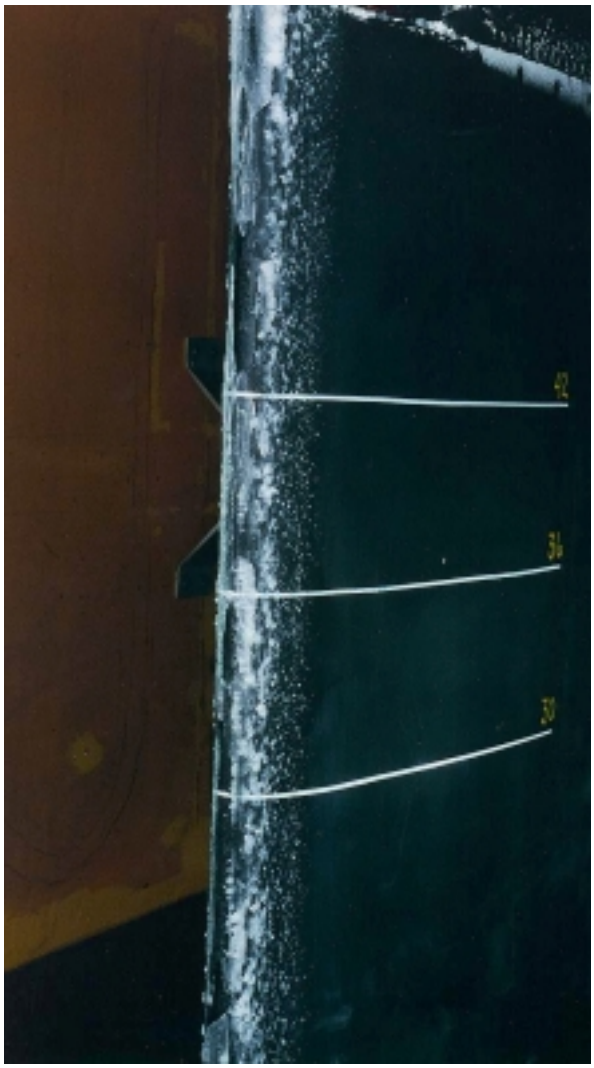

Fig. 1 Inter-cycle ice accretion.

Fig. 2 Failure-mode glaze ice accretion.

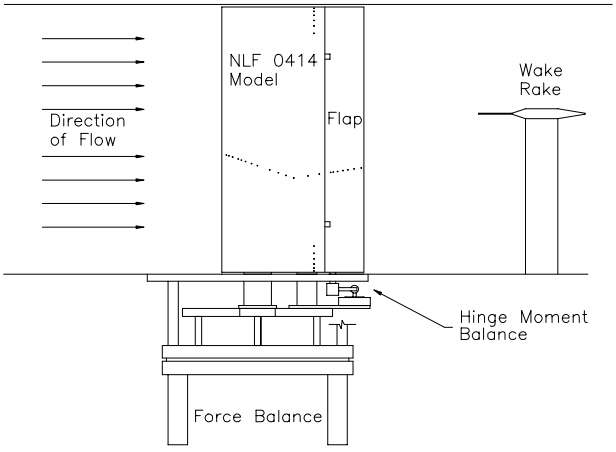

Fig.3 Schematic of the experimental setup.

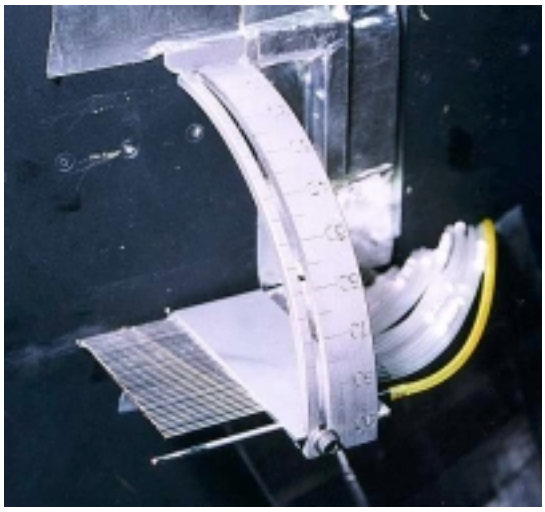

Fig. 4 Boundary-layer mouse.

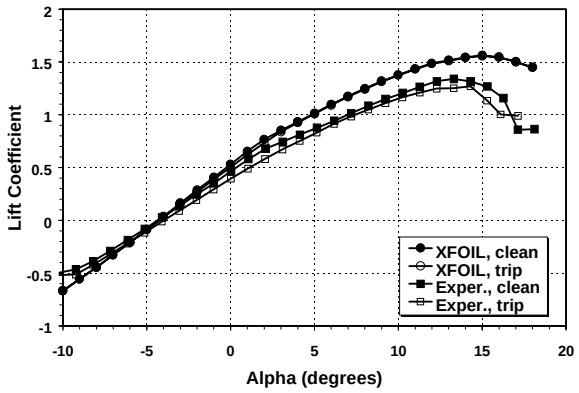

5 a) C_λ vs α

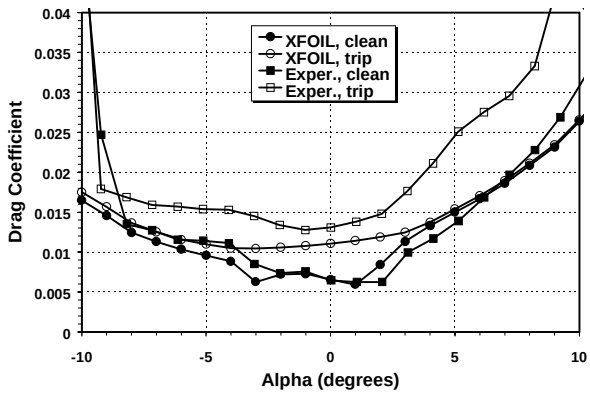

5 b) C_d vs α

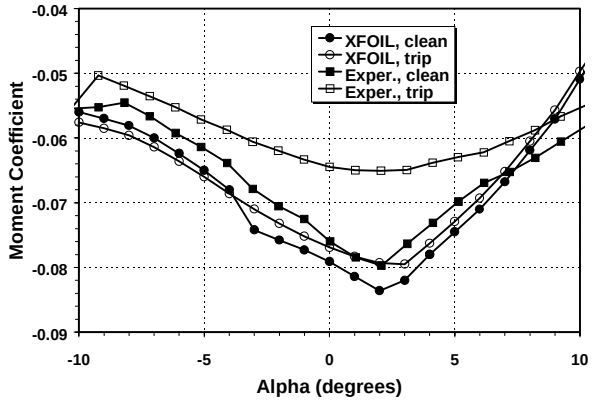

5 c) C_m vs α

Fig. 5 NLF(1)-0414F airfoil performance with and without boundary-layer trip (Re =1.80 x 10^6).

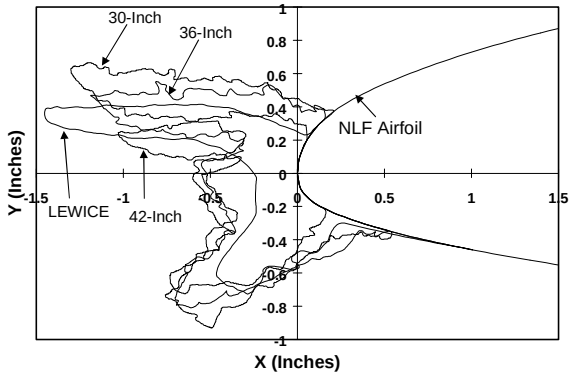

Fig. 6 IPS failure case glaze ice accretions and LEWICE prediction.

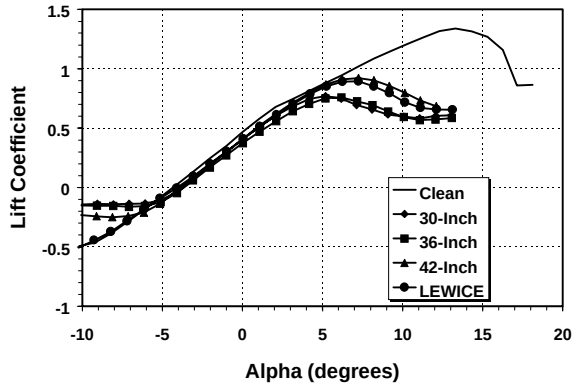

7 a) C_λ vs α

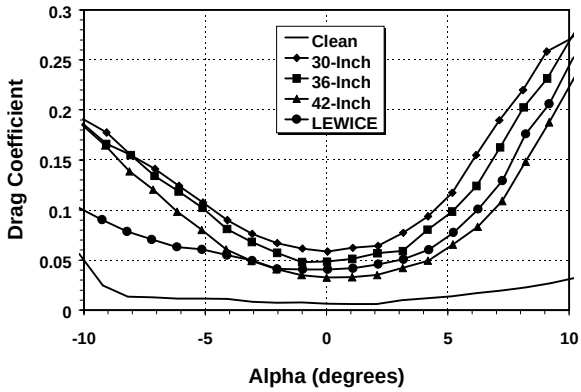

7 b) C_d vs α

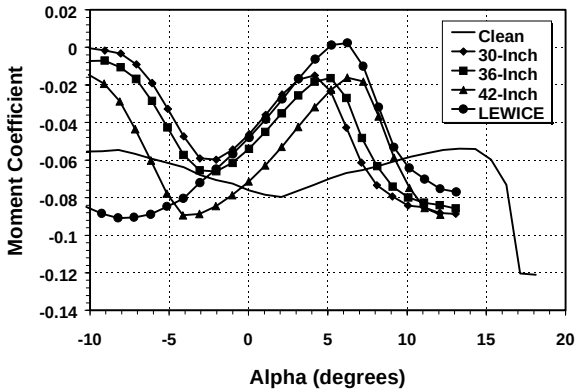

7 c) C_m vs α

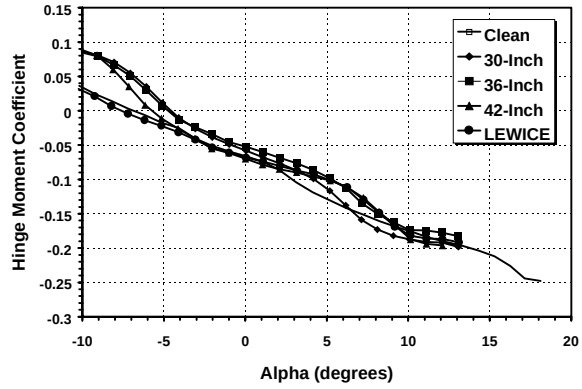

7 d) C_h vs α

Fig. 7 NLF(1)-0414F airfoil performance with IPS failure case glaze ice (Re =1.80 x 10^6).

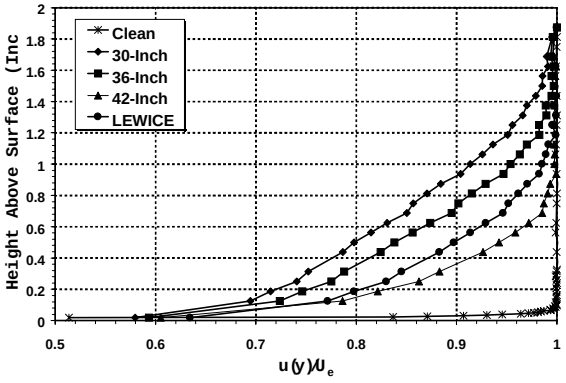

Fig. 8 Boundary-layer profiles for IPS failure case glaze ice (α = 0°, Re =1.80 x 10^6).

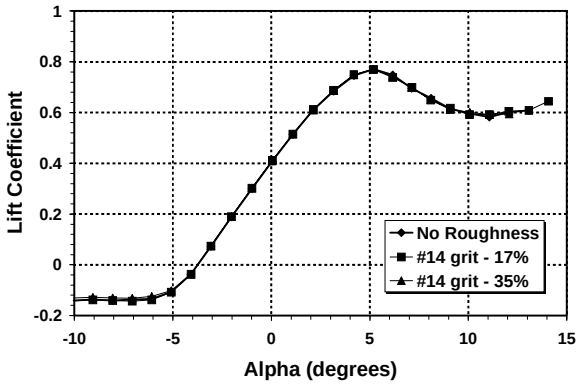

Fig. 9 NLF(1)-0414F lift with 30-inch IPS failure ice case with and without roughness (Re=1.80x10^6).

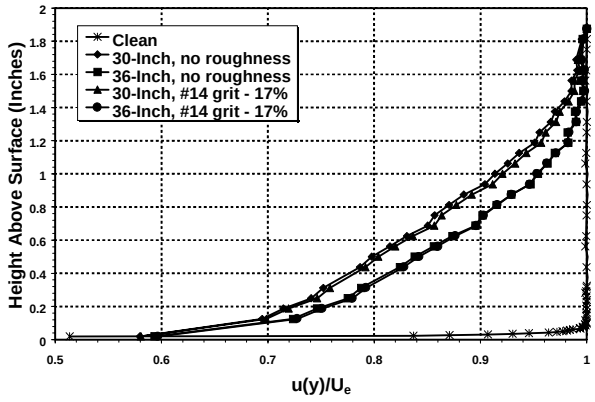

Fig. 10 Boundary-layer profiles for 30 and 36-inch IPS failure case w/wo roughness (α = 0°, Re =1.80 x 10^6).

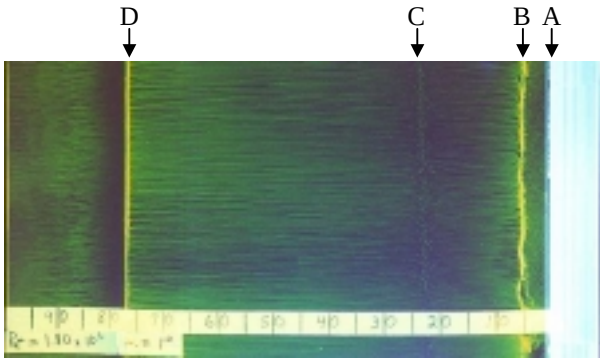

Fig. 11 Flow visualization 30-inch IPS failure-case (note flow right to left, α = 1°, Re =1.80 x 10^6).

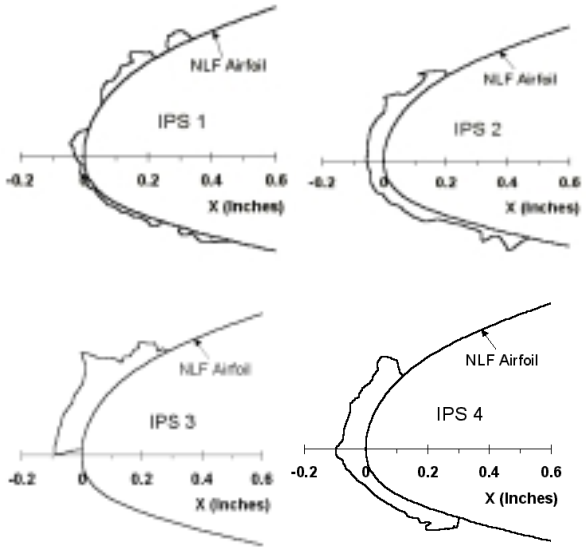

Fig. 12 Inter-cycle ice accretions.

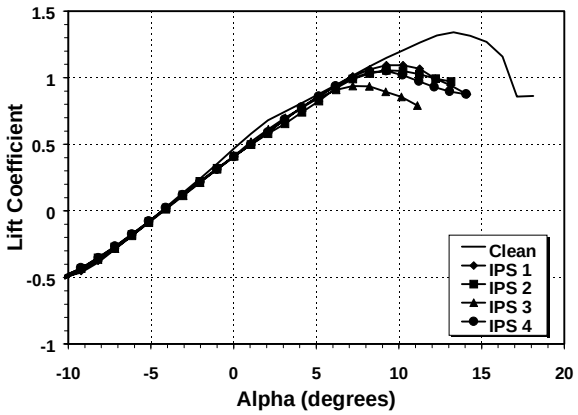

13 a) C_λ vs α

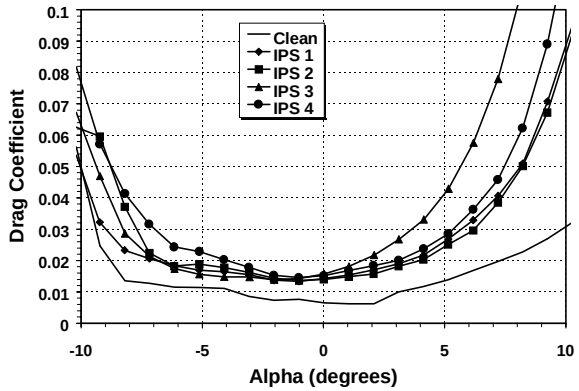

13 b) C_d vs α

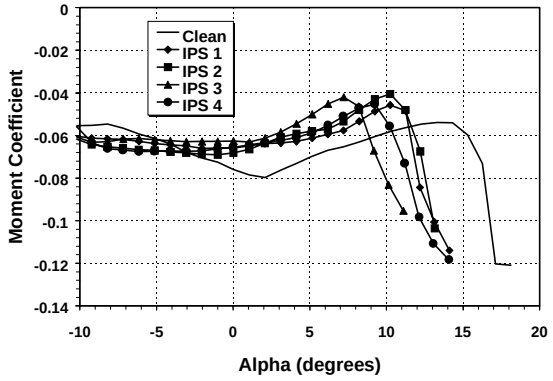

13 c) C_m vs α

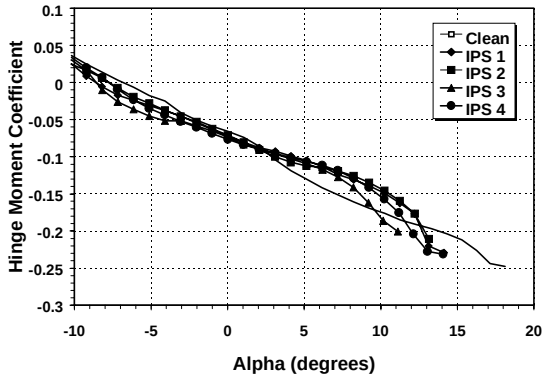

13 d) C_h vs α

Fig. 13 NLF(1)-0414F airfoil performance with inter-cycle ice accretions (Re =1.80 x 10^6)

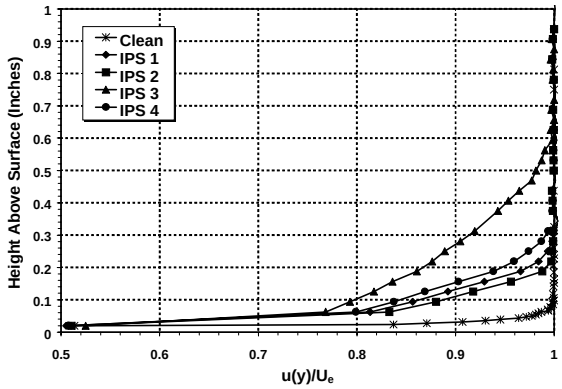

Fig. 14 Boundary-layer profiles for inter-cycle ice accretions with roughness (α = 0°, Re =1.80 x 10^6).

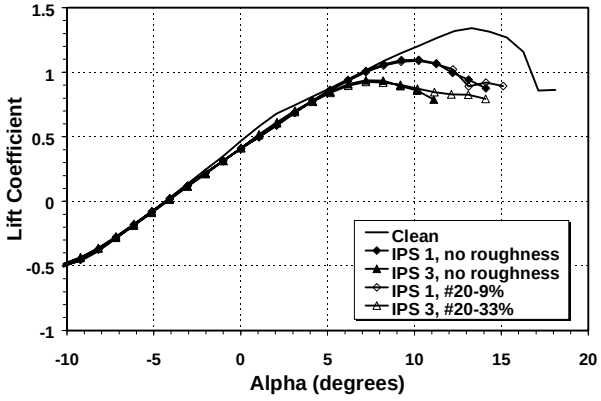

Fig 15 NLF(1)-0414F lift performance with inter-cycle ice accretions w/wo roughness (Re =1.80 x 10^6).

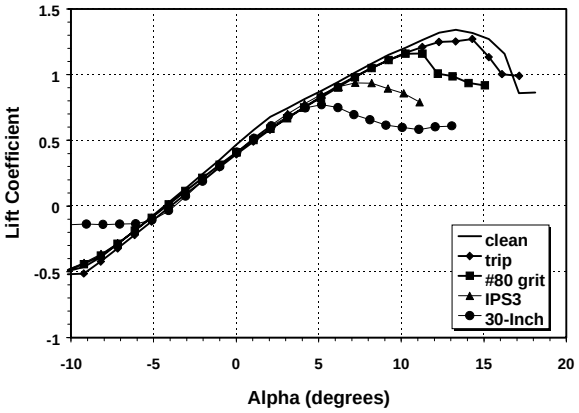

16 a) C_λ vs α

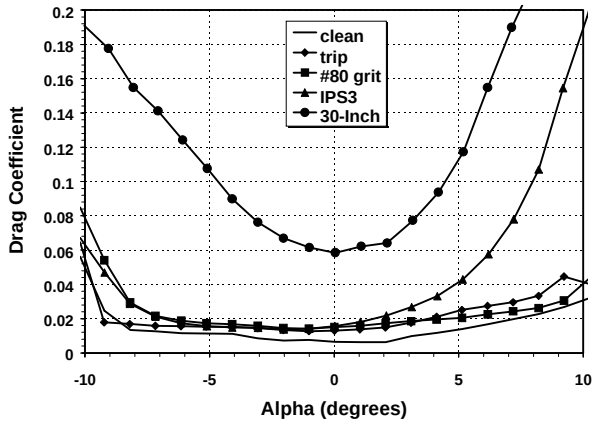

16 b) C_d vs α

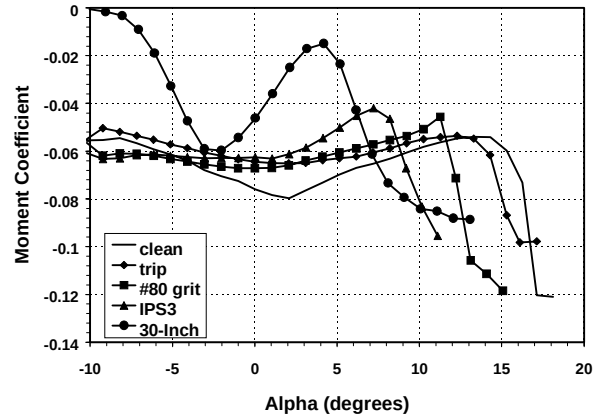

16 c) C_m vs α

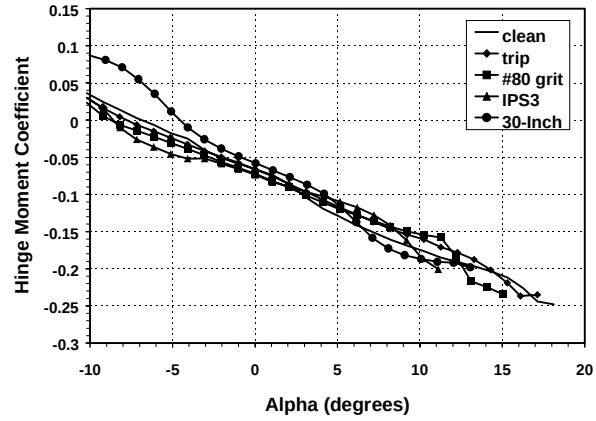

16 d) C_h vs α

Fig. 16 NLF(1)-0414F airfoil performance summary with roughness and ice simulations (Re =1.80 x 10^6)